www.ietdl.org

Published in IET Power Electronics
Received on 10th May 2013
Revised on 6th August 2013
Accepted on 26th August 2013
doi: 10.1049/iet-pel.2013.0365

ISSN 1755-4535

# Control loop design of sequential switching shunt regulator considering the influence of double section functioning

*Fang Li, Xiaojie You, Yan Li*

*Institute of Electrical Engineering, School of Electrical Engineering, Beijing Jiaotong University, Beijing 100044, People's Republic of China*
*E-mail: hahalifang@163.com*

**Abstract:** Sequential switching shunt regulator (S3R) has been widely used in satellites for its simple structure and high reliability. Double section functioning, which has two sections operating simultaneously, is the other operating mode of S3R beside the normal mode. It is inevitable and can lead to larger bus voltage ripple, less controllability and higher switching losses. A detailed analysis based on the double section functioning process description is given on the boundary load current, the main bus voltage ripple and the switching frequency. Considering the influence of double section functioning, a new method of control loop design of S3R is proposed based on the small single mathematical model. A 4.5 kW S3R prototype is built to verify the control loop design, and the load region of double section functioning can be limited as designed.

## 1 Introduction

Solar array regulator is an important part of power conditioning unit (PCU) in the satellites' power system [1–5]. Sequential switching shunt regulator (S3R) was firstly introduced by D. O'Sullivan in 1977. Several derivative topologies are proposed afterwards, such as sequential switching shunt series regulator (S4R), S3R–digital shunt regulator (S3R–DSR) and sequential switching shunt maximum power point regulator (S3 MPPR) [6–12]. All these derivative topologies have the similar characteristics with S3R.

Owing to the hysteresis control of S3R and integration effect of main error amplifier (MEA), S3R can operate in double section functioning mode (over commutation mode) in some load regions, in which main bus is regulated by two sections simultaneously instead of one section [13, 14]. Double section functioning has several effects, such as lower power quality, which can be characterised by an increase in bus voltage ripple, lower controllability and higher switching losses. This operation mode is inevitable because that switching frequency of shunt switch is low when the load consumption is near to a multiple of the current of one solar array, and that PI controller is normally chosen as MEA in regulated bus to eliminate steady-state error. Therefore load region in double section functioning mode must be limited in an acceptable range.

To obtain the good performance of S3R, the control loop design should be studied after analysing the influence of double section functioning. The simulation and test results of double section functioning are given in [13]. This paper also points out that over communications are especially responsible for an increase of the ripple, so it is important to make sure that these modes do not cause a ripple above the specifications. In [14], the effect of parasitic capacitance on double section functioning is represented, and it also describes that double section functioning can cause the drawbacks such as higher switching frequency, larger bus voltage ripple and poor electromagnetic compatibility (EMC) performance [15]. Although the modelling and control loop design of S3R can be learned from the derived structures which are similar to S3R. In earlier studies, relationships of basic circuit parameters were given in [16], and the steady state and small signal models of power stage of the new conditioner like S3R were proposed [17]. Then, system model of S4R is analysed in [18, 19], in which a simple linearisation of non-linear transconductances is obtained. The control loop design of S4R is also given based on this system model in [20]. In recent years, the control loop gain of S3R–DSR considering the delay casing by parasitic capacitance is analysed in [8, 21]. A detailed dynamic analysis and exhaustive guidelines for S3R design are given in [22], as well as the resonance between the SA section and its harness. Although these papers mainly research on the model and design of S3R from different aspects, they do not propose the design method to limit the effect on double section functioning of S3R system.

The purpose of this paper is to analyse double section functioning specifically, such as the boundary load current, main bus voltage ripple and switching frequency, based on description of the processes. A new control loop design method of S3R is proposed to limit the load region in double section functioning mode. This paper is organised

as follows: Seciton 2 gives an introduction to S3R and processes of double section functioning; Section 3 analyses the performances of S3R in normal mode and in double section functioning mode, respectively; Section 4 proposes the small-single mathematical model of S3R system and the control loop design. The experimental results are presented in Section 5, and the conclusions are given in Section 6.

## 2 Processes of double section functioning

### 2.1 Introduction of S3R

Schematic diagram of S3R is shown in Fig. 1. Solar arrays are divided into $n$ identical parts, and each part corresponds to a shunt regulator (called one section). All of the output ports are parallel and connected to the capacitor array $C_{\text{bus}}$. The voltage of main bus $v_{\text{bus}}$ is sampled (factor is $K$) and regulated by PI compensator of MEA to produce control signal $v_{\text{MEA}}$. $v_{\text{MEA}}$ compares with different reference voltages $V_{\text{ref\_}m}$ to generate drive signals $V_{\text{G\_}m}$ of shunt switches. $i_{\text{L}}$ is the total load current of S3R.

As $V_{\text{ref\_}m}$ of different hysteresis comparators (bang-bang comparators) distribute in different levels, MEA hysteresis bands are increasing sequentially. Hence, in steady state, only one section is operating in switching mode, whereas others are remaining on or off constantly. Different division methods of hysteresis bands are shown in Fig. 2 [14, 18, 19]. It is more difficult for two sections to influence each other for hysteresis bands with dead-zone, whereas with overlapping S3R can expand hysteresis bands to restrain the failure operation of the regulating section caused by noises. The latter method is more often used in engineering, and

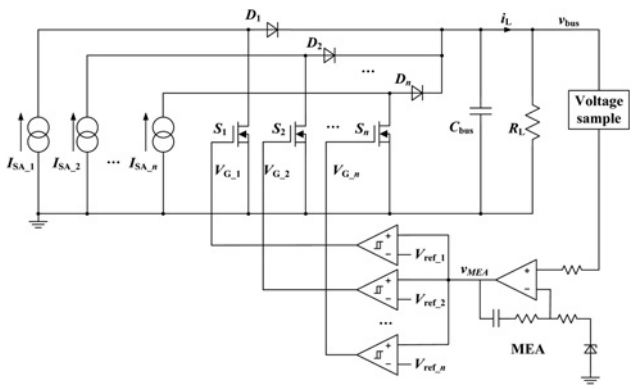


**Fig. 1** *Schematic diagram of S3R*

the upper and lower thresholds of the adjacent sections meet

$$V_{hh} = V_{ll} = \frac{V_{h\_n} - V_{l\_1} - V_{hl}}{n-1} \tag{1}$$

Switching frequency $f$ is given in [14, 16, 23], and the function of $f$ on load current $i_{\text{load}}$ is shown as

$$f(i_{\text{load}}) = \frac{i_{\text{load}}(I_{\text{SA}} - i_{\text{load}})}{\Delta V_{\text{bus}} C_{\text{bus}} I_{\text{SA}}} = \frac{-i_{\text{load}}^2 + I_{\text{SA}} i_{\text{load}}}{\Delta V_{\text{bus}} C_{\text{bus}} I_{\text{SA}}} \tag{2}$$

The maximum switching frequency follows

$$f_{\max} = \frac{I_{\text{SA}}}{4\Delta V_{\text{bus}} C_{\text{bus}}} \tag{3}$$

In which, $I_{\text{SA}}$ is the output current of one SA part, $i_{\text{load}}$ is output current of the regulating section and satisfying $0 < i_{\text{load}} < I_{\text{SA}}$. $\Delta V_{\text{bus}}$ is the main bus voltage ripple in normal mode. Therefore the maximum switching frequency is limited by the parameters of S3R system. That is why the operating mode of S3R is called the limit cycle [24].

### 2.2 Processes of double section functioning

From (2), we can obtain that switching period of regulating section is near infinity when $i_{\text{load}} \simeq 0$ or $i_{\text{load}} \simeq I_{\text{SA}}$. Owing to integration of MEA, $v_{\text{MEA}}$ is accumulating in the long time and may trigger the adjacent section's hysteresis bond. Then two sections are operating in switching mode simultaneously, that is, double section functioning. However, expanding hysteresis bands of $v_{\text{MEA}}$ with overlapping aggravates the appearance of double section functioning.

In this mode, the two sections are influencing each other and the waveforms of $v_{\text{MEA}}$ and $v_{\text{bus}}$ are varying when the load current changes. The simulation waveforms are shown in Figs. 3*c*–*g* and *h*. $v_{\text{MEA}}$ changes between $V_{l\_1}$ and $V_{h\_2}$, and the main bus voltage ripples are higher than that of normal mode.

We can draw the conclusion that there are two modes of S3R, one is normal mode, and the other is double section functioning mode. The load regions of two modes are varying when the parameters of S3R are different.

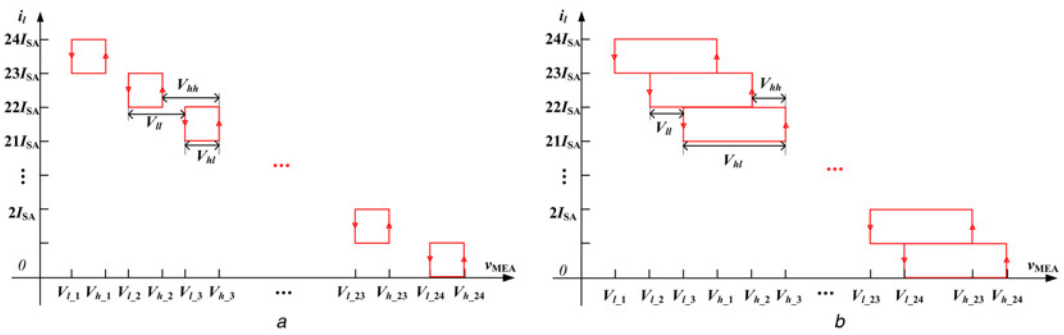


**Fig. 2** *MEA hysteresis bands of different sections in S3R a* with dead-zone *b* with overlapping

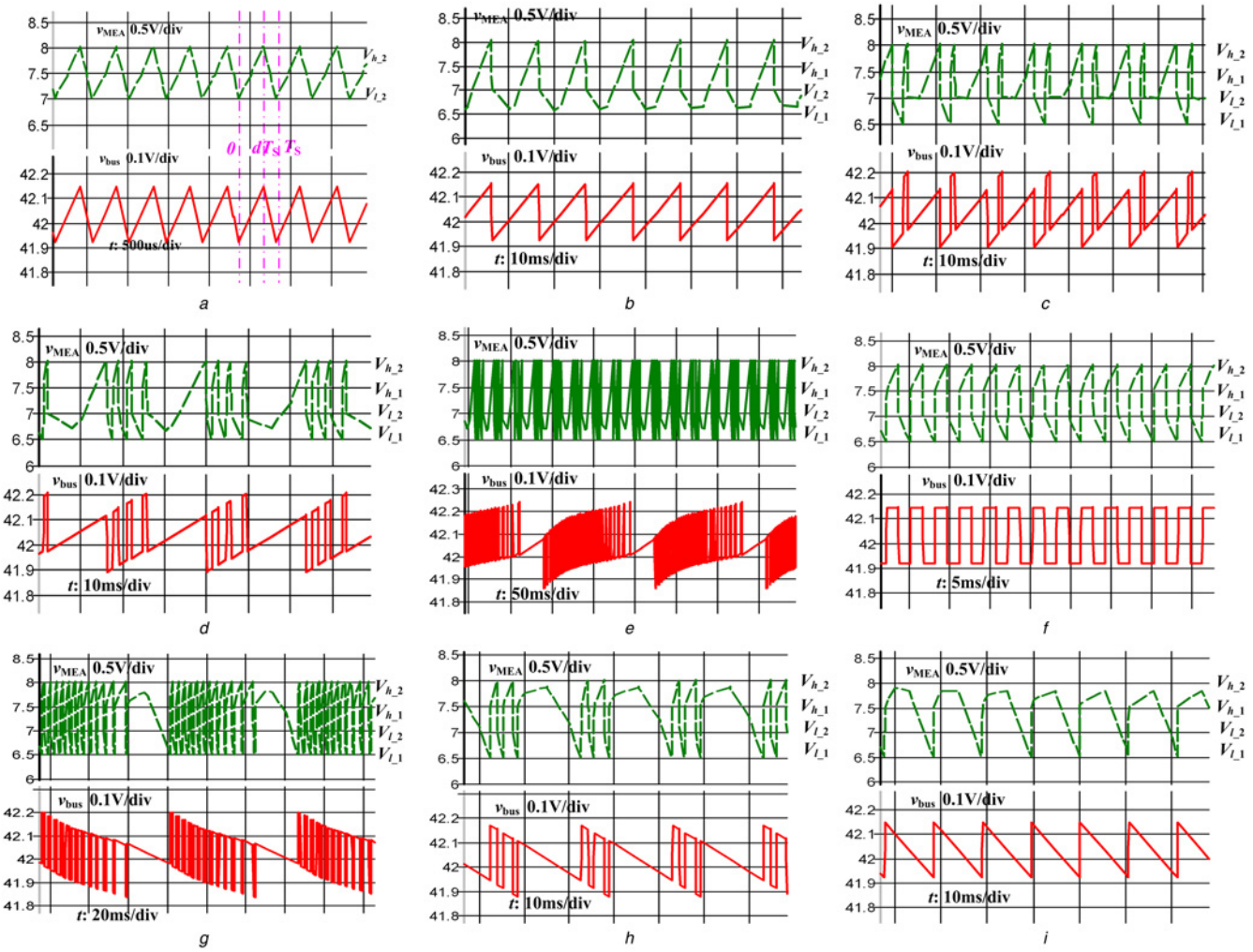


**Fig. 3** *Simulation waveforms of S3R*

*a–b* and *i* Waveforms in normal mode
*c–g* and *h* Waveforms in double section conditioning mode

## 3 Operation modes of S3R

### 3.1 Normal mode

Define $I_b$ as the boundary load current between two modes, so S3R operates in normal mode when $I_b < i_{\text{load}} < I_{\text{SA}} - I_b$. In Fig. 3*a*, the duty cycle $d$ is the ratio of output diode conduction time to total switching period $T_{\text{S}}$.

At $t = 0$, shunt switch turns off. Hence, during [0, $dT_{\text{S}}$], shunt switch is off and diode is on, $v_{\text{bus}}$ is increasing with slope $m = (I_{\text{SA}} - i_{\text{load}})/C_{\text{bus}}$ and $v_{\text{MEA}}$ is increasing up to trigger $V_{h\_2}$, the higher threshold of the hysteresis band. At $dT_{\text{S}}$, shunt switch turns on. Then during [$dT_{\text{S}}$, $T_{\text{S}}$], the solar array is shunted, $v_{\text{bus}}$ is decreasing with slope $m = -i_{\text{load}}/C_{\text{bus}}$ and $v_{\text{MEA}}$ is decreasing to $V_{l\_2}$. At $T_{\text{S}}$, shunt switch turns off again. Hence, in steady state, $v_{\text{bus}}$ is regulated in ripple zone $\Delta V_{\text{bus}}$ through the switching of shunt switch, and the average value of $v_{\text{bus}}$ is $V_{\text{bus}}$.

In normal mode, the capacitor array charges and discharges in each cycle, and $\Delta V_{\text{bus}}$ is [23]

$$\Delta V_{\text{bus}} = \frac{t_{\text{on}}(I_{\text{SA}} - i_{\text{load}})}{C_{\text{bus}}} = \frac{t_{\text{off}} i_{\text{load}}}{C_{\text{bus}}} \tag{4}$$

In the past researches, only the proportion effect of MEA was taken into account to make linear approximation. The relationship between $V_{hl}$ and $\Delta V_{\text{bus}}$ is

$$KA_P \Delta V_{\text{bus}} = V_{hl} \tag{5}$$

Then, charging time $t_{\text{off}}$ and discharging time $t_{\text{on}}$ of the capacitor array can be calculated, and the sum of them is switching period $T_{\text{s}}$. The switching frequency is shown as (2). Changing processes of $v_{\text{MEA}}$, $t_{\text{off}}$ and $t_{\text{on}}$ at different load currents are illustrated in Figs. 5*a* and *b*.

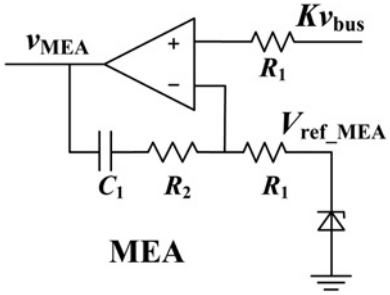


**Fig. 4** *Circuit of MEA compensator*




doi: 10.1049/iet-pel.2013.0365

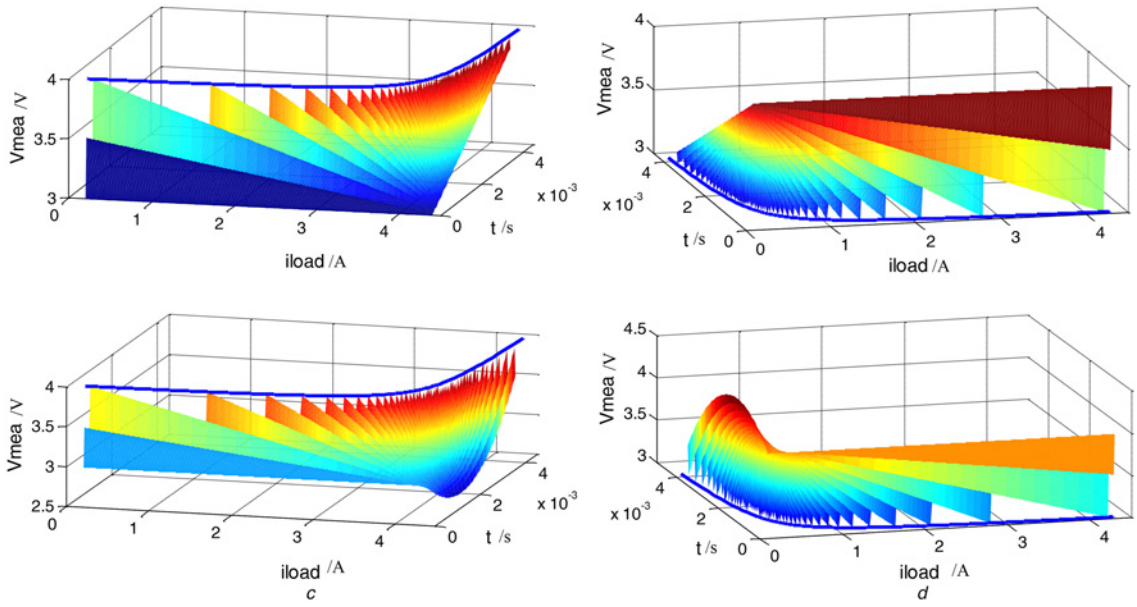


**Fig. 5** *Switching times and changing processes of $v_{MEA}$ at different load currents in normal mode*

*a* $t_{on}$ and $v_{MEA}$ under linear approximation
*b* $t_{off}$ and $v_{MEA}$ under linear approximation
*c* $t_{on}$ and $v_{MEA}$ with no approximation
*d* $t_{off}$ and $v_{MEA}$ with no approximation

However, a different analysis will be made when considering integration effect of MEA as well. Fig. 4 is the circuit of the MEA compensator.

During [0, $dT_S$], input and output signals of MEA compensator follows

$$v_{MEA}(0) = Kv_{bus}(0) + \left(Kv_{bus}(0) - V_{ref\_MEA}\right)\frac{R_2}{R_1} + v_{c1}(0) \tag{6}$$

$$v_{MEA}(t) = Kv_{bus}(t) + \left(Kv_{bus}(t) - V_{ref\_MEA}\right)\frac{R_2}{R_1} + v_{c1}(0) + \frac{1}{C_1}\int_0^t \frac{\left(Kv_{bus}(t) - V_{ref\_MEA}\right)}{R_1}\mathrm{d}t \tag{7}$$

$v_{bus}$ satisfies

$$v_{bus}(0) = V_{bus} + V_e \tag{8}$$

$$v_{bus}(t) = v_{bus}(0) + mt = V_{bus} + V_e + mt \tag{9}$$

$V_e$ is the deviation voltage value between actual and average value of main bus, $m$ is changing slope and $V_{bus}$ meets $KV_{bus} = V_{ref\_MEA}$. The instantaneous value of $v_{MEA}$ is

$$v_{MEA}(t) = \frac{1}{2}KA_PA_Imt^2 + \left[K\left(A_P + 1\right)m + V_eKA_PA_I\right]t + v_{MEA}(0) \tag{10}$$

The function between $v_{MEA}$ and $t$ is quadratic and $v_{MEA}$ is not only related to $K$ and $A_p$ as (5), but also determined by $A_I$, $V_e$ and $m$.

In Fig. 3*a*, $V_e(0) = -\Delta V_{bus}/2$, $v_{MEA}(0) = V_{l\_2}$, $v_{MEA}(dT_S) = V_{h\_2}$, then $V_e(dT_S) = \Delta V_{bus}/2$, $v_{MEA}(T_S) = V_{l\_2}$. Two equations about $v_{MEA}$, $i_{load}$, $t_{on}$ and $t_{off}$ can be founded. Changing processes of $v_{MEA}$, $t_{off}$ and $t_{on}$ at different load currents are shown in Figs. 5*c* and *d*. From former analysis, it is obviously that the processes of $v_{MEA}$ are different under linear approximation. Especially at $i_{load} \simeq 0$ or $i_{load} \simeq I_{SA}$, $v_{MEA}$ may trigger adjacent section's hysteresis band. However, $t_{off}$ and $t_{on}$ are the same with the former analysis under linear approximation.

### 3.2 Double section functioning mode

To simplify the analysis, assume that there are only two sections in the S3R. S3R is operating in double section functioning mode when $I_{SA} - I_b \le i_L \le I_{SA} + I_b$, as shown in Figs. 3*c–h*. The total output current of S3R changes among the value of $I_{SA}$, $2I_{SA}$ and 0, $v_{MEA}$ changes among the value of $V_{h\_2}$, $V_{l\_2}$, $V_{h\_1}$ and $V_{l\_1}$. The waveform of $v_{bus}$ is no longer triangle but varying with the total load current.

*3.2.1 Boundary load current:* From (10) and Fig. 3*b*, when $i_L < I_{SA}$ MEA signal has minimum value

$$v_{MEA\_min}(i_L) = -\frac{\left[K\left(A_P + 1\right)\left((I_{SA} - i_L)/C_{bus}\right) + V_eKA_PA_I\right]^2}{2KA_PA_I\left((I_{SA} - i_L)/C_{bus}\right)} + v_{MEA}(0) \tag{11}$$

At boundary load current $I_b$, $v_{MEA}(0) = V_{l\_2}$ and $v_{MEA\_min} = V_{l\_1}$. $I_{SA} - i_L$ can be solved and the lower value is

$$I_b = \frac{-b - \sqrt{b^2 - 4ac}}{2a} \tag{12}$$

in which

$$a = \left(\frac{K(A_P+1)}{C_{\text{bus}}}\right)^2,$$

$$b = -\frac{2V_{ll}KA_PA_I}{C_{\text{bus}}} - \frac{\Delta V_{\text{bus}}K^2(A_P+1)A_PA_I}{C_{\text{bus}}},$$

$$c = \left(\frac{\Delta V_{\text{bus}}KA_PA_I}{2}\right)^2$$

The derivative of $I_b$ on $A_I$ is positive, the load current range in double section functioning becomes larger with the increase of $A_I$, and its influence cannot be neglected any more.

In the case when $i_L$ is bigger than $I_{\text{SA}}$, S3R operates symmetrically to the case when $i_{\text{L}}$ is smaller than $I_{\text{SA}}$ according to the operation principle. Therefore the load region of double section functioning has two boundary currents, and the absolute value are the same. The valid interval of Figs. 5*c* and *d* is $I_b \le i_{\text{load}} \le I_{\text{SA}} - I_b$, when S3R is operating in normal mode. The minimum switching frequency in normal mode follows

$$f_{\min} = \frac{I_b(I_{\text{SA}} - I_b)}{\Delta V_{\text{bus}} C_{\text{bus}} I_{SA}} \tag{13}$$

*3.2.2 Main bus voltage ripple:* Fig. 6 is the amplification of waveforms in double section functioning mode when $I_{\text{SA}} - I_b \le i_L \le I_{\text{SA}}$. The expression of $\Delta V_{\text{bus\_DSF}}$ is given as below. Its derivation process can be referred in the Appendix.

$$\Delta V_{\text{bus\_DSF}}(i_L) = 2\Delta V_{\text{bus}} - \frac{\sqrt{2}\left(\sqrt{V_{ll}} + \sqrt{V_{ll}+V_{hl}}\right)}{\sqrt{KA_PA_IC_{\text{bus}}}}\sqrt{I_{\text{SA}} - i_L} \tag{14}$$

The smaller $I_{\text{SA}} - i_L$ is, the bigger $\Delta V_{\text{bus\_DSF}}$ will be. However, at $i_L = I_{\text{SA}}$, the ripple of $v_{\text{bus}}$ is near $\Delta V_{\text{bus}}$, and the waveform of bus voltage is similar to square wave, as shown in Figs. 3*f*. Hence, $\Delta V_{\text{bus\_DSF}}$ is the biggest when $I_{\text{SA}} - i_L$ is slightly larger than zero, and corresponding to the minimum load current step d*i* is the maximum value of $\Delta V_{\text{bus\_DSF}}$.

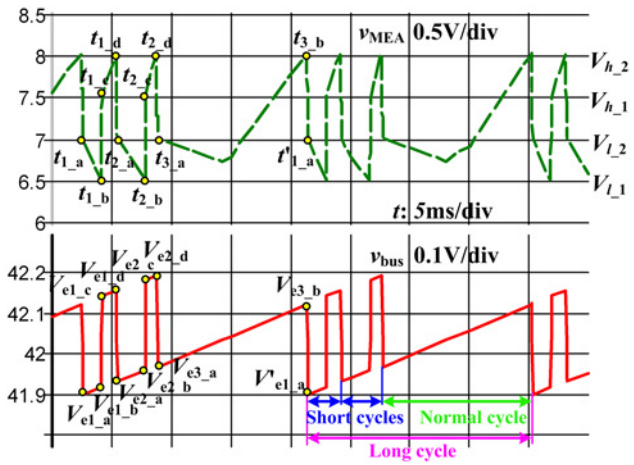


**Fig. 6** *Amplification of the waveforms in double section functioning mode*

*3.2.3 Switching frequency:* The time intervals of $[t_{1\_b}, t_{1\_c}]$ and $[t_{1\_d}, t_{2\_a}]$ are both very short, and $v_{\text{bus}}$ changes by $\Delta V_{\text{bus}}$ and $-\Delta V_{\text{bus}}$. If ignoring these intervals, $v_{\text{bus}}$ may increase with the slope $m = (I_{\text{SA}} - i_L)/C_{\text{bus}}$ during $[t_{1\_a}, t_{2\_a}]$, as well as $[t_{1\_a}, t_{3\_b}]$, as shown in Fig. 6.

$$t_{3\_b} - t_{1\_a} = \frac{\Delta V_{\text{bus}}}{m} = \frac{\Delta V_{\text{bus}} C_{\text{bus}}}{I_{\text{SA}} - i_L} \tag{15}$$

During $[t_{3\_b}, t'_{1\_a}]$, $v_{\text{bus}}$ changes $-\Delta V_{\text{bus}}$, and

$$t'_{1\_a} - t_{3\_b} = \frac{-\Delta V_{\text{bus}}}{m} = \frac{\Delta V_{\text{bus}} C_{\text{bus}}}{i_L} \tag{16}$$

From (15) and (16), we can see that the period of the long cycle from $t_{1\_a}$ to $t'_{1\_a}$ is similar to (4). That is why $t_{\text{off}}$ and $t_{\text{on}}$ under two analyses in Fig. 5 are approximate.

Meanwhile, in Fig. 6 there are many short cycles in double section functioning mode. The accurate numerical computation of each short cycle period can be calculated according to the Appendix. Since the computation is complicated, we can simplify that during $[t_{1\_a}, t_{1\_b}]$ and $[t_{1\_c}, t_{1\_d}]$ $v_{\text{bus}}$ remain unchanged and $V_{e1\_a} + \Delta V_{\text{bus}} = V_{e1\_c}$, then

$$v_{\text{MEA}}(t) \simeq V_e KA_PA_I t + v_{\text{MEA}}(0) \tag{17}$$

$v_{\text{MEA}}$ and $V_{\text{bus}}$ can be given by

$$\begin{cases} v_{\text{MEA}}(t_{1\_b}) \simeq V_{e1\_a}KA_PA_I(t_{1\_b} - t_{1\_a}) + v_{\text{MEA}}(t_{1\_a}) \\ v_{\text{MEA}}(t_{1\_b}) \simeq V_{e1\_a}KA_PA_I(t_{1\_d} - t_{1\_c}) + v_{\text{MEA}}(t_{1\_c}) \\ V_{e1\_a} + \Delta V_{\text{bus}} = V_{e1\_c} \end{cases} \tag{18}$$

Approximately, the short cycle of $[t_{1\_a}, t_{2\_a}]$ is

$$t_{2\_a}(V_{e1\_a}) - t_{1\_a}(V_{e1\_a}) \simeq -\frac{V_{ll}\Delta V_{\text{bus}}}{KA_PA_I(V_{e1\_a}^2 + \Delta V_{\text{bus}}V_{e1\_a})} \tag{19}$$

When $V_{e1\_a} = \Delta V_{\text{bus}}/2$, the minimum period of short cycles is

$$(t_{2\_a} - t_{1\_a})_{\min} = \frac{4V_{ll}}{V_{hl}A_I} \tag{20}$$

The period of Fig. 3*f* when $i_L = I_{\text{SA}}$ and and $V_{e1\_a} = \Delta V_{\text{bus}}/2$ is given by (20). The switching loss in double section functioning mode is almost twice of the loss in normal mode. Therefore the maximum frequency of short cycle should be less than $f_{\max}/2$

$$f_{\text{DSF\_max}} = \frac{V_{hl}A_I}{4V_{ll}} \le \frac{f_{\max}}{2} \tag{21}$$




doi: 10.1049/iet-pel.2013.0365

## 4 Modelling and control loop design

### 4.1 Small-single mathematical model

From Fig. 3*a*, define $D$ as the average value of $d$, $I_{\text{load}}$ as the average value of $i_{\text{load}}$, we obtain

$$D = \frac{I_{\text{load}}}{I_{\text{SA}}} \tag{22}$$

The function of $D$ on $V_{\text{MEA}}$ (the average value of $v_{\text{MEA}}$ in normal mode) is

$$D = \frac{V_{\text{MEA}} - V_{l\_m}}{V_{hl\_m}} \tag{23}$$

By introducing small signal disturbance, we can obtain

$$D + \hat{d} = \frac{(V_{\text{MEA}} + \hat{v}_{\text{MEA}}) - V_{l\_m}}{V_{hl\_m}} \tag{24}$$

so

$$\hat{d} = \frac{\hat{v}_{\text{MEA}}}{V_{hl\_m}} \tag{25}$$

Set, $i_{\text{SA}} = I_{\text{SA}} + \hat{i}_{\text{SA}}$, $v_{\text{bus}} = V_{\text{bus}} + \hat{v}_{\text{bus}}$, $d = D + \hat{d}$, and the small-signal transfer function of S3R power stage is shown as follows by using state–space averaging method

$$\frac{\hat{v}_{\text{bus}}}{\hat{d}}|_{\hat{i}_{\text{SA}}=0} = \frac{R_{\text{load}} I_{\text{SA}}}{(R_{\text{load}} C_{\text{bus}} s + 1)} \tag{26}$$

Therefore S3R power stage is a first-order inertial system, which is stable and only has a left-half plane pole as shown in Fig. 9*a*. The small-signal mathematical model of S3R power stage is drawn in the dashed rectangle in Fig. 7.

Adding hysteresis comparator control section and power stage together, then we can obtain the transconductance $G = I_{\text{SA}}/V_{hl\_m}$. Note that $G$ is the transconductance corresponding to $V_{hl}$ [14], not $V_{hh}$ in [22] or total approximation in [18, 19]. Because that the change of $v_{\text{MEA}}$ is $V_{hl}$ in normal mode. However, $v_{\text{MEA}}$ changes between two sections in double section functioning mode. Considering $I_b$ is very small and the period of long cycle is similar to the period in normal mode, the transconductance in double section functioning mode can be treated as in normal mode approximately.

The transfer function of MEA in Fig. 4 is $A(s) = A_P(1 + A_I/s) + 1$, which can be simplified as $A(s) = A_P(1 + A_I/s)$ because of $A_P \gg 1$. S3R closed loop small-signal mathematical model with $v_{\text{bus}}$ sampling factor ($K$) and MEA is shown in Fig. 7.

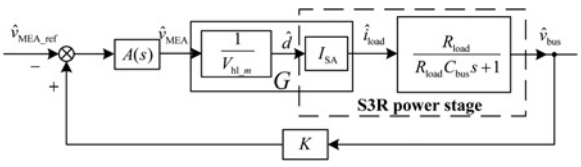


**Fig. 7** *Small-signal mathematical model of S3R*

The open loop transfer function of main bus voltage close loop is

$$H(s) = KA_P\left(1 + \frac{A_I}{s}\right) G \frac{R_{\text{load}}}{1 + R_{\text{load}} C_{\text{bus}} s} \tag{27}$$

S3R is a second-order system and turning frequencies of open loop gain are $\omega_Z = A_I$ and $\omega_P = 1/R_{\text{load}}C_{\text{bus}}$.

### 4.2 Control loop characteristics

*4.2.1 Magnitude and phase characteristics:* S3R open loop gain can be simplified as $H(s) = KA_{\text{P}}GR_{\text{load}}/(R_{\text{load}}C_{\text{bus}}s + 1)$ without integration part [25]. The cut-off frequency is $\omega_C \simeq KGA_P/C_{\text{bus}}$. The frequency response of the magnitude and phase of $H(s)$ are shown in Figs. 9*c* and *d*. Phase margin is approximately 90° and magnitude margin is infinite in ideal case. It verifies that S3R system is stable.

*4.2.2 Output impedance:* By setting $i_{\text{load}} = 0$ in Fig. 7, we obtain Fig. 8 [23, 25]. Hence, the output impedance can be approximated as follows

$$\begin{aligned} Z_{\text{o}}(s) &= \frac{\hat{v}_{\text{bus}}(s)}{\hat{i}_{\text{load}}(s)} = \frac{(1/C_{\text{bus}}s)}{1 + (KA(s)G/C_{\text{bus}}s)} \\ &\simeq \frac{1}{C_{\text{bus}}} \frac{s}{(s + \omega_Z)(s + \omega_C)} \end{aligned} \tag{28}$$

Therefore the maximum output impedance is

$$Z_{\text{o\_max}} = \frac{1}{KA_PG} \tag{29}$$

The frequency response of the magnitude of output impedance is shown in Fig. 9*e*.

### 4.3 Control loop design

S3R parameters are: the main bus voltage $V_{\text{bus}}$, the main bus voltage sample factor $K$, single solar array output current $I_{\text{SA}}$, solar array sections $n$, $v_{\text{MEA}}$ range $V_{l\_1} \sim V_{h\_n}$, the maximum bus voltage ripple $V_{\text{ripple}}$, the maximum output impedance $Z_{\text{o\_max}}$, the maximum switching frequency $f_{\text{max}}$, the minimum load current regulation d$i$ and the boundary load current $I_b$.

S3R control loop design considering double section functioning should follow the guidelines:

First determine $K = V_{\text{ref\_MEA}}/V_{\text{bus}}$. From (29) we can obtain

$$\frac{1}{KA_PG} = \frac{V_{hl}}{KA_PI_{SA}} \le Z_{\text{o\_max}} \tag{30}$$

Substituting (5) into (30), $\Delta V_{\text{bus}}$ in normal mode, yielding

$$\Delta V_{\text{bus}} \le Z_{\text{o\_max}} I_{SA} \tag{31}$$

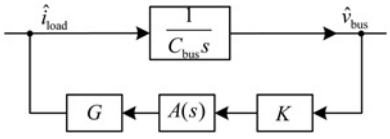


**Fig. 8** *Output impedance mathematical model of S3R*

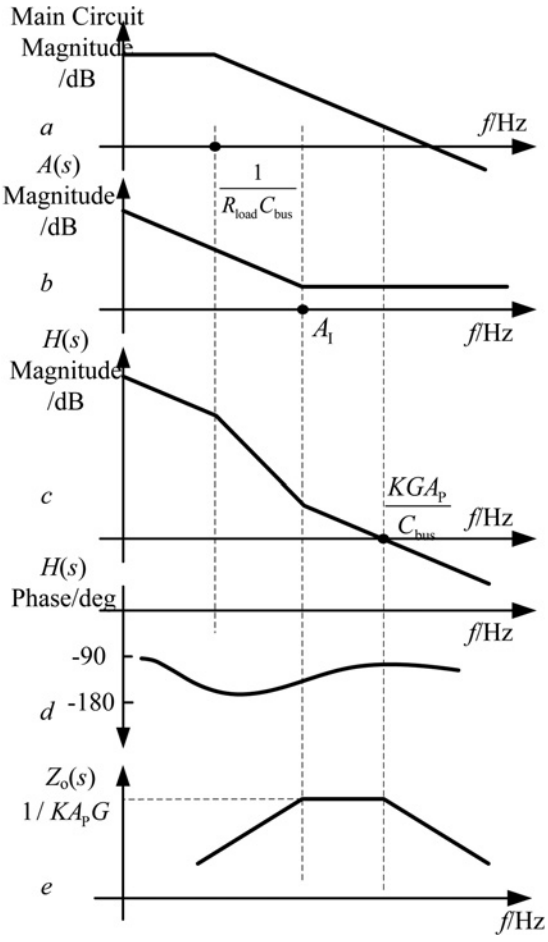


**Fig. 9** *Frequency responses of S3R*

*a* Magnitude of S3R power stage
*b* Magnitude of $A(s)$
*c* and *d* Magnitude and phase of $H(s)$
*e* Magnitude of $Z_o(s)$

The maximum switching frequency meets (3), and it is better to be less than the cutoff frequency $\omega_C \simeq KGA_PG/C_{\text{bus}}$.

$$\frac{I_{\text{SA}}}{4\Delta V_{\text{bus}} C_{\text{bus}}} \le f_{\max} \le \frac{\omega_C}{2\pi} = \frac{KA_PG}{2\pi C_{\text{bus}}} \tag{32}$$

$C_{\text{bus}}$ should satisfy

$$\frac{I_{\text{SA}}}{4\Delta V_{\text{bus}} f_{\max}} \le C_{\text{bus}} \le \frac{KA_PG}{2\pi f_{\max}} \tag{33}$$

If there is no solution of (33), a tradeoff is chosen as $C_{\text{bus}} \ge I_{\text{SA}}/4\Delta V_{\text{bus}} f_{\max}$ and the noise of switching frequency cannot be inhibited. Initially identify one value of $C_{\text{bus}}$, then calculate $\omega_C = KA_PG/C_{\text{bus}}$. Usually integration parameter $A_I = \omega_Z$ is chosen as one-tenth of the cutoff frequency $\omega_C$.

From above, we can obtain

$$\frac{1}{Z_{\text{o\_max}} K} \le A_PG = \frac{I_{\text{SA}}}{K\Delta V_{\text{bus}}} \tag{34}$$

The hysteresis bands is given by

$$\begin{cases} \dfrac{V_{h\_n} - V_{l\_1}}{n} \le V_{hl} < V_{h\_n} - V_{l\_1} \\ \dfrac{V_{hl} A_I}{4V_{ll}} \le \dfrac{f_{\max}}{2} \end{cases} \tag{35}$$

The interval of optimal solution of $G$ is

$$\begin{cases} \dfrac{I_{\text{SA}}}{V_{h\_n} - V_{l\_1}} < G \le \dfrac{nI_{\text{SA}}}{V_{h\_n} - V_{l\_1}} \\ G \ge \dfrac{I_{\text{SA}}\left(A_I(n-1) + 2f_{\max}\right)}{2f_{\max}\left(V_{h\_n} - V_{l\_1}\right)} \end{cases} \tag{36}$$

Select one value of $G$ then $A_P$ can be solved. Finally, substitute all parameters into (12) and (14) to check whether the demands can be reached or not. If not, make a slight modification to $C_{\text{bus}}$ and $G$, and recalculate until all demands are satisfied.

## 5 Experimental results

To verify the control loop design of S3R system, a 4.5 kW laboratory prototype is built. The system parameters are $V_{\text{bus}} = 42$ V, $I_{\text{SA}} = 4.5$ A, $n = 24$, $V_{\text{ripple}} = 500$ mV, $Z_{\text{o\_max}} = 50\text{m}\Omega$, $f_{\max} = 3$ kHz.

By setting a suitable margin, the system parameters are chosen as: $\Delta V_{\text{bus}} \le 220$ mV, $81.6\text{ Hz} \le f \le 2.5$ kHz, $Z_{\text{o\_max}} = 48.6\ \text{m}\Omega$ in normal mode. $I_b = 4\,0$ mA and the

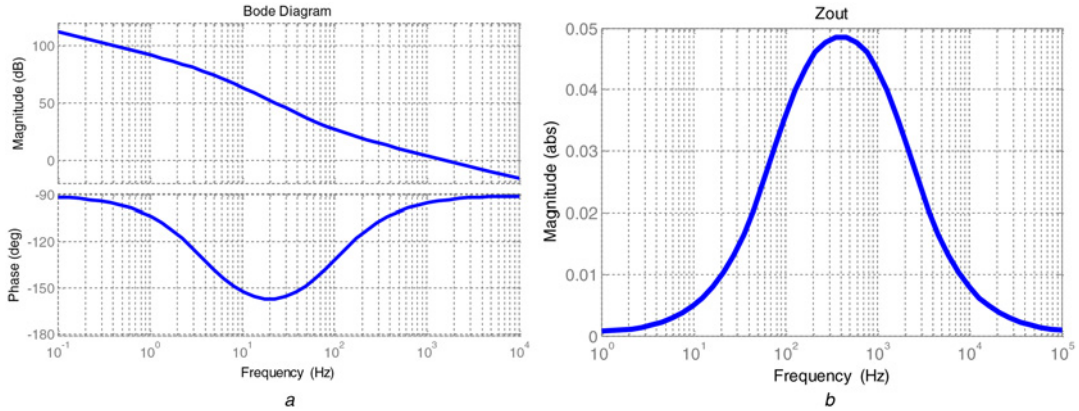


**Fig. 10** *Frequency responses of S3R*

*a* Magnitude and phase of the open loop transfer function
*b* Magnitude of output impedance




doi: 10.1049/iet-pel.2013.0365

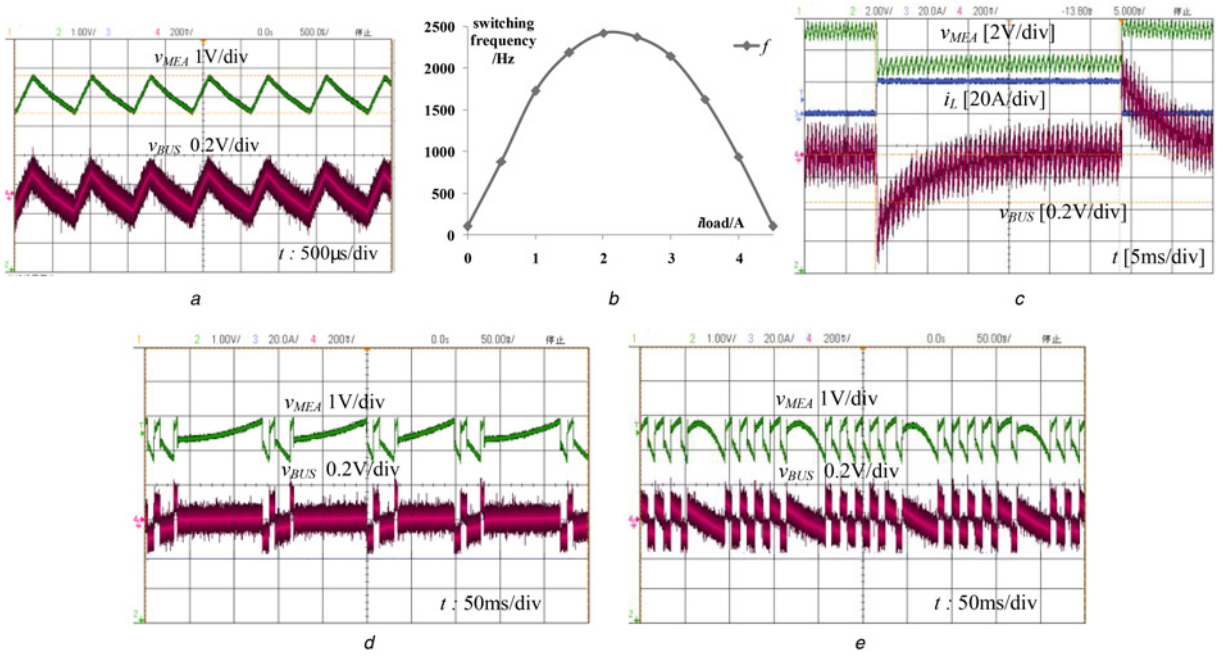


**Fig. 11** *Experimental results*

*a* In normal mode
*b* Switching frequency of regulating section
*c* Waveforms at 20 A load step
*d* and *e* Waveforms in double section functioning mode

maximum value of $\Delta V_{\text{bus\_DSF}}$ is 330 mV in double section functioning mode.

Figs. 10*a* and *b* are the bode plot of the open loop transfer function and magnitude of output impedance drown by MATLAB when switching frequency is the highest at $i_L = I_{SA}/2$. The result is similar with theoretical analysis, and the maximum output impedance is $< 50\ \text{m}\Omega$.

Experimental results of the prototype are shown in Figs. 11*a–e*, in normal mode $\Delta V_{\text{bus}}$ is 240 mV, the maximum switching frequency is <2.5 kHz. Fig. 11*c* shows the waveforms at 20 A load current step, the overshoot of $v_{\text{bus}}$ is 600 mV and the adjusting time is near 1 ms. It can be seen that S3R can track the change of the load quickly and accurately. The load current range of double section functioning is ±40 mA, the maximum bus voltage ripple is 360 mV, $f_{\text{eq\_max}}$ is 550 Hz, waveforms is shown in Figs. 11*d* and *e*.

## 6 Conclusion

In this paper, the influence of double section functioning of S3R has been analysed in detail, including the boundary load current of load region, the bus voltage ripple and the switching frequency. Based on S3R closed loop small-signal mathematical model, a new method of control loop design considering the double section functioning is proposed in this paper. Finally, the experimental results show the excellent correlation with theoretical analysis. In double section functioning mode of the 4.5 kW S3R prototype, the load region is less than ±1% of the current of one solar array, the biggest bus voltage ripple is 1.5 times the ripple in normal mode but still under the specification, and the frequency is less than half the maximum frequency. S3R, designed by the method proposed in this paper, can operate well in both normal mode and double section functioning mode.

## 7 Acknowledgments

This work was supported by The Specialized Research Fund for the Doctoral Program of Higher Education of China (award number 20110009120032) and a Class General Financial Grant from the China Postdoctoral Science Foundation (award number 2011M500225).

## 8 References

1 Patel, M.R.: ' Spacecraft power system' (CRC Press, 2005)
2 Capel, A., O'Sullivan, D., Marpinard, J.C.: 'High-power conditioning for space applications', *Proc. IEEE*, 1988, **76**, (4), pp. 391–408
3 Soubrier, L., Trehet, E.: 'High power PCU for Alphabus: PSR100 V'. Proc. Ninth European Space Power Conf. (ESPC), Saint Raphael, France, June 2011
4 Castiaux, J.P., Bury, P., Liegeois, B.: 'Power conditioning units for high power geostationary satellites'. Power Electronics Specialists Conf., 28th Annual IEEE PESC, St. Louis, MO, 22–27, June 1997, vol. 1, pp. 722–733
5 Garrigós, A., Carrasco, J.A., Blanes, J.M., García de Quirós, F., Sanchis-Kilders, E.: 'A power conditioning unit for high power GEO satellites based on the sequential switching shunt series regulator'. Electrotechnical Conf., 2006. MELECON IEEE, Mediterranean, Malaga, 16–19 May 2006, pp. 1186–1189
6 O'Sullivan, D., Weinberg, A.H.: 'The Sequential switching shunt regulator (S3R)'. Third Estec Spacecraft Power Conditioning Seminar, Noordwijk, Netherlands, 21–23 September 1977 (ESA SP–126, pp. 123–131)
7 Capel, A., Perol, P.: 'Comparative performance evaluation between the S4R and the S3R regulated bus topologies'. Power Electronics Specialists Conf., IEEE PESC. 32nd Annual vol. 4, Vancouver, BC, June 2001, pp. 1963–1969
8 Blanes, J.M., Garrigós, A., Carrasco, J.A., Weinberg, A.H., Weinberg, S.: 'S3R optimization for high parasitic capacitance solar arrays'. Proc. Eighth European Space Power Conf. (ESPC), Constance, Germany, 14–19 September 2008
9 Maset1, E., Sanchis-Kilders1, E., Ejea1, J.B., *et al.*: 'New high power/high voltage battery-free bus for electrical propulsion in satellites'. Proc. Power Electronic Specialists Conf., 2007 38th IEEE PESC, Orlando, FL, 17–21 June 2007, pp. 1391–1397

10 Garrigos, A., Blanes, J.M., Carrasco, J.A., Weinberg, A.H., Caballero, G., Soto, A.: 'Maximum power point tracking for GEO telecommunication satellites'. Proc. Eighth European Space Power Conf. (ESPC), Constance, Germany, 14–19 September 2008

11 Blanes, J.M., Garrigós, A., Carrasco, J.A., *et al.*: 'Sequential switching shunt maximum power point regulator (S3MPPR)'. Proc. Ninth European Space Power Conf. (ESPC), Saint Raphael, France, June 2011

12 Maset, E., Sanchis-Kilders, E., Weinberg, A.H., Bta Ejea, J., Ferreres, A., Blanes, J.M., Garrigos, A., Carrasco, J.A.: 'Ion drive propulsion MPP power conditioning system without battery'. Proc. Eighth European Space Power Conf. (ESPC), Constance, Germany, 14–19 September 2008

13 Picart, G., Michoud, V.: 'Behavioral modeling of the SPACEBUS 3000 power conditioning unit'. Proc. Fourth European Space Power Conf. (ESPC), Poitiers, France, 4–8 September, 1995, pp. 89–94

14 Zhu, H.Y., Zhang, D.L.: 'Influence of multijunction Ga/As solar array parasitic capacitance in S3R and solving methods for high-power applications', *IEEE Trans. Power Electron.*, 2014, **29**, (1), pp. 179–190

15 Jensen, H.: 'Shunt regulator module'. Proc. Eighth European Space Power Conf. (ESPC), Constance, Germany, 14–19 September 2008

16 Kuwajima, S., Sato, T., Tsuya, N., Kobayashi, M., Okamura, T., Honda, Y.: 'Digital sequential shunt regulator for solar power conditioning of engineering test satellite'. Power Electronics Specialists Conf., 19th Annual IEEE PESC, Kyoto, Japan, 11–14 April 1988, pp. 619–625

17 Shivanna, G.: 'A new universal spacecraft power conditioner'. Proc. Fourth European Space Power Conf. (ESPC), Poitiers, France, 4–8 September, 1995, pp. 41–45

18 Garrigós, A., Carrasco, J.A., Rubiato, J., Avila, E., Blanes, J.M., Sanchis kilders, E.: 'System model of the S4R regulator for spacecraft regulated high power busses'. Proc. 35th IEEE Power Electronics Specialists Conf., Aachen, Germany, 2004, pp. 2645–2650

19 Garrigós, A., Carrasco, J.A., Blanes, J.M., Sanchis, E.: 'Modeling the sequential switching shunt series regulator', *IEEE Power Electron. Lett.*, 2005, **3**, (1), pp. 7–13

20 Garrigós, A., Rubiato, J., Carrasco, J.A., Blanes, J.M., Ferreres, A.: 'Control loop design of the sequential switching shunt series regulator'. Electrotechnical Conf., MELECON IEEE, Mediterranean, Malaga, 16–19 May 2006, pp. 1194–1197

21 Blanes, J.M., Garrigós, A., Carrasco, J.A., Sanchis, E., Maset, E.: 'New parallel power processing strategy for the sequential shunt switching regulator'. 13th EPE Conf. on European Power Electronics and Applications, Barcelona, 8–10 September 2009, pp. 1–10

22 Delepaut, C.: 'S3R stability margins and design guidelines'. Proc. Eighth European Space Power Conf. (ESPC), Constance, Germany, 14–19 September 2008

23 Zhiyun, B., Hongyu, Z., Mingyan, W.: 'Low output impedance solar array shunt regulator based on S3R topology'. Proc. Chinese Society for Electrical Engineering (CSEE), December 30, 2010, vol. 30 supplement, pp. 192–198

24 Zhao, C.Z.: 'Technology of solar array shunt-regulation on spacecraft', *Spacecr. Eng.*, 2009, **18**, (3), pp. 41–47

25 O'Sullivan, D.: 'Space power electronics – design drivers', *ESA J.*, 1994, **18**, pp. 1–23


## 9 Appendix

This appendix is provided to derive the main bus voltage ripple in double section functioning mode.

There are many short cycles and a normal cycle in the long cycle of double section functioning. By setting the minimum point of bus voltage $t_{1\_a}$ is the beginning of the long cycle, the next minimum point $t'_{1\_a}$ is the end of the long cycle. In the short cycle, two sections turn on and off, such as $[t_{1\_a}, t_{2\_a}]$, $[t_{2\_a}, t_{3\_a}]$ in Fig. 6. In the normal cycle $[t_{1\_a}, t_{2\_a}]$, only one section turns on and off.

$[t_{1\_a}, t_{1\_b}]$, $S_1$ on, $D_1$ off, $S_2$ off, $D_2$ on, $v_{\mathrm{MEA}}(t_{1\_a}) = V_{l\_2}$, $v_{\mathrm{MEA}}(t_{1\_b}) = V_{l\_1}$, $v_{\mathrm{bus}}(t_{1\_a}) = V_{\mathrm{bus}} + V_{e1\_a}$, the slope of $v_{\mathrm{bus}}$ is $m_1 = (I_{\mathrm{SA}} - i_L)/C_{\mathrm{bus}}$. (see (37))

$[t_{1\_b}, t_{1\_c}]$, $S_1$ off, $D_1$ on, $S_2$ off, $D_2$ on, $v_{\mathrm{MEA}}(t_{1\_b}) = V_{l\_1}$, $v_{\mathrm{MEA}}(t_{1\_c}) = V_{h\_1}$, $v_{\mathrm{bus}}(t_{1\_b}) = V_{\mathrm{bus}} + V_{e1\_b}$, the slope of $v_{\mathrm{bus}}$ is $m_2 = (2I_{\mathrm{SA}} - i_L)/C_{\mathrm{bus}}$. This time span is very little, by using linear approximation, we obtain

$$\begin{cases} t_{1\_c} - t_{1\_b} = \dfrac{C_{\mathrm{bus}}\Delta V_{\mathrm{bus}}}{2I_{\mathrm{SA}} - i_L} = \dfrac{C_{\mathrm{bus}}}{2I_{\mathrm{SA}} - i_L}\dfrac{V_{hl}}{KA_P} \\ V_{e1\_c} - V_{e1\_b} = \Delta V_{\mathrm{bus}} = \dfrac{V_{hl}}{KA_P} \end{cases} \tag{38}$$

$[t_{1\_c}, t_{1\_d}]$, $S_1$ off, $D_1$ on, $S_2$ on, $D_2$ off, $v_{\mathrm{MEA}}(t_{1\_c}) = V_{h\_1}$, $v_{\mathrm{MEA}}(t_{1\_d}) = V_{h\_2}$, $v_{\mathrm{bus}}(t_{1\_c}) = V_{\mathrm{bus}} + V_{e1\_c}$, the slope of $v_{\mathrm{bus}}$ is $m_3 = m_1 = (I_{\mathrm{SA}} - i_L)/C_{\mathrm{bus}}$. (see (39))

$[t_{1\_d}, t_{2\_a}]$, $S_1$ on, $D_1$ off, $S_2$ on, $D_2$ off, $v_{\mathrm{MEA}}(t_{1\_d}) = V_{h\_2}$, $v_{\mathrm{MEA}}(t_{2\_a}) = V_{l\_2}$, $v_{\mathrm{bus}}(t_{1\_d}) = V_{\mathrm{bus}} + V_{e1\_d}$, the slope of $v_{\mathrm{bus}}$ is $m_4 = (-i_L)/C_{\mathrm{bus}}$. By using linear approximation, we obtain

$$\begin{cases} t_{2\_a} - t_{1\_d} = \dfrac{C_{\mathrm{bus}}\Delta V_{\mathrm{bus}}}{-i_L} = \dfrac{C_{\mathrm{bus}}}{-i_L}\dfrac{V_{hl}}{KA_P} \\ V_{e2\_a} - V_{e1\_d} = \Delta V_{\mathrm{bus}} = \dfrac{V_{hl}}{KA_P} \end{cases} \tag{40}$$

$[t_{2\_a}, t_{3\_a}]$ is similar to $[t_{1\_a}, t_{2\_a}]$.

$[t_{3\_a}, t_{3\_b}]$, $S_1$ on, $D_1$ off, $S_2$ off, $D_2$ on, $v_{\mathrm{MEA}}(t_{3\_a}) = V_{l\_2}$, $v_{\mathrm{MEA}}(t_{3\_b}) = V_{h\_2}$, $v_{\mathrm{bus}}(t_{3\_a}) = V_{\mathrm{bus}} + V_{e3\_a}$, the slope of $v_{\mathrm{bus}}$ is $m_1 = (I_{\mathrm{SA}} - i_L)/C_{\mathrm{bus}}$. (see (41))

$$\begin{cases} t_{1\_b} - t_{1\_a} = \dfrac{-\left[K(A_P+1)m_1 + V_{e1\_a}KA_PA_I\right] - \sqrt{\left[K(A_P+1)m_1 + V_{e1\_a}KA_PA_I\right]^2 - 2KA_PA_Im_1(V_{l\_1} - V_{l\_2})}}{KA_PA_Im_1} \\ V_{e1\_b} - V_{e1\_a} = m_1(t_{1\_b} - t_{1\_a}) \end{cases} \tag{37}$$

$$\begin{cases} t_{1\_d} - t_{1\_c} = \dfrac{-\left[K(A_P+1)m_1 + V_{e1\_c}KA_PA_I\right] - \sqrt{\left[K(A_P+1)m_1 + V_{e1\_c}KA_PA_I\right]^2 - 2KA_PA_Im_1(V_{h\_2} - V_{h\_1})}}{KA_PA_Im_1} \\ V_{e1\_d} - V_{e1\_c} = m_3(t_{1\_d} - t_{1\_c}) \end{cases} \tag{39}$$

$$\begin{cases} t_{3\_b} - t_{3\_a} = \dfrac{-\left[K(A_P+1)m_1 + V_{e3\_a}KA_PA_I\right] - \sqrt{\left[K(A_P+1)m_1 + V_{e3\_a}KA_PA_I\right]^2 - 2KA_PA_Im_1(V_{h\_2} - V_{l\_2})}}{KA_PA_Im_1} \\ V_{e3\_b} - V_{e3\_a} = m_1(t_{3\_b} - t_{3\_a}) \end{cases} \tag{41}$$




doi: 10.1049/iet-pel.2013.0365

The minimum of $v_{\mathrm{MEA}}$ in $[t_{3\_a}, t_{3\_b}]$ must satisfy

$$v_{\mathrm{MEA\_min}} > V_{l\_1} \tag{42}$$

$[t_{3\_b}, t'_{1\_a}]$, $S_1$ on, $D_1$ off, $S_2$ on, $D_2$ off, $v_{\mathrm{MEA}}(t_{3\_b}) = V_{h\_2}$, $v_{\mathrm{MEA}}(t_{1\_c}) = V_{l\_2}$, $v_{\mathrm{bus}}(t'_{1\_a}) = V_{\mathrm{bus}} + V_{e3\_b}$, the slope of $v_{\mathrm{bus}}$ is $m_4 = (-i_L)/C_{\mathrm{bus}}$. By using linear approximation, we obtain

$$\begin{cases} t'_{1\_a} - t_{3\_b} = \dfrac{C_{\mathrm{bus}}\Delta V_{\mathrm{bus}}}{-i_L} = \dfrac{C_{\mathrm{bus}}}{-i_L}\dfrac{V_{hl}}{KA_P} \\ V'_{e1\_a} - V_{e3\_b} = \Delta V_{\mathrm{bus}} = \dfrac{V_{hl}}{KA_P} \end{cases} \tag{43}$$

The biggest main bus voltage ripple is $\Delta V_{\mathrm{bus\_DSF}} = V_{e2\_d} - V_{e1\_a}$ etc. $2\Delta V_{\mathrm{bus}} - (V_{e3\_b} - V_{e3\_a})$. By setting the minimum of $v_{\mathrm{MEA}}$ in $[t_{3\_a}, t_{3\_b}]$ as $V_{l\_1}$ to simplify the calculation, $V_{e3\_b}$ and $V_{e3\_a}$ are given by

$$\begin{cases} v_{\mathrm{MEA\_min}} = V_{l\_1} \\ v_{\mathrm{MEA}}(t_{e3\_b}) = V_{h\_2} \\ V_{e3\_b} - V_{e3\_a} = m_1(t_{3\_b} - t_{3\_a}) \end{cases} \tag{44}$$

Then $V_{e3\_b} - V_{e3\_a}$ is

$$V_{e3\_b} - V_{e3\_a} = \frac{\sqrt{2}\left(\sqrt{V_{ll}} + \sqrt{V_{ll} + V_{hl}}\right)}{\sqrt{KA_PA_IC_{\mathrm{bus}}}}\sqrt{I_{\mathrm{SA}} - i_L} \tag{45}$$

The function between $\Delta V_{\mathrm{bus\_DSF}}$ and $i_L$ is

$$\Delta V_{\mathrm{bus\_DSF}}(i_L) = 2\Delta V_{\mathrm{bus}} - \frac{\sqrt{2}\left(\sqrt{V_{ll}} + \sqrt{V_{ll} + V_{hl}}\right)}{\sqrt{KA_PA_IC_{\mathrm{bus}}}}\sqrt{I_{\mathrm{SA}} - i_L} \tag{46}$$